Article | Received 22 July 2025; Revised 27 August 2025; Accepted 2 September 2025; Published 18 September 2025
https://doi.org/10.55092/aimat20250013

Crystallographic insights into the hydrogen barrier mechanism of polyethylene furanoate (PEF) for high-pressure storage applications: comparison with polyamide 6 and polyethylene

Zhen Liu[1,†], Yaolin Guo[2,†,*], Bin Gu[3], Nianxiang Qiu[4,*], Xiaojing Bai[5], Yifan Li[6], Zheyu Hu[7], Muhammad Adnan[8] and Yajie Zhang[2]

[1] Ningbo Key Laboratory of High Performance Petroleum Resin Preparation Engineering and Technology, Ningbo Polytechnic, Ningbo 315800, China

[2] Ningbo Institute of Materials Technology & Engineering, Chinese Academy of Sciences, Ningbo 315201, China

[3] The First Aircraft Institute, AVIC, Xi'an 710072, China

[4] Yangtze Delta Region Institute (Huzhou), University of Electronic Science and Technology, Huzhou 313001, China

[5] School of Materials Science and Engineering, Anyang Institute of Technology, Anyang 455000, China

[6] College of Materials Science and Chemical Engineering, Harbin Engineering University, Harbin 150001, China

[7] School of Materials Science and Engineering, China University of Petroleum (East China), Qingdao 266580, China

[8] University of Chinese Academy of Sciences, Beijing 100049, China

† These authors contributed equally to this work.

* Correspondence author; E-mail: guoyaolin@nimte.ac.cn (Y.G.); qiunianxiang@csj.uestc.edu.cn (N.Q.).

Highlights:

- PEF demonstrates a notably greater diffusion energy barrier at 0.828 eV, approximately 2.9 times that of PA6 and 26 times that of PE, indicating remarkable resistance to hydrogen passage.
- The infiltration barrier of 0.772 eV surpasses PA6 by 20%, while the effusion barrier, at 0.555 eV, is 3.2 times higher than that of PA6, establishing a two-fold kinetic obstacle for H_2.
- Illustrates how a co-planar formation of four oxygen atoms strengthens diffusion resistance by introducing additional energy barriers.

Abstract: This work examines the hydrogen barrier capabilities of the crystalline α-PEF relative to α-PA6 and α-PE through MD simulations using a revised CVFF force field benchmarked against DFT calculations.

Although minor deviations persist in chain-level details, our MD model successfully reproduces the key crystallographic and energetic properties of α-PEF, including lattice constants, surface energy, and NEB barriers. DFT results show that α-PEF exhibits superior polymorphic stability under pressure, with a potential stress-induced transition from α' to α. MD simulations reveal weak hydrogen physisorption in the three materials, but PEF shows relatively stronger adsorption at low temperatures due to the oxygen-rich surface, accompanied by enhanced van der Waals and coulombic interactions with H_2. According to NEB calculations, particularly, PEF consistently possesses the highest H_2 migration barriers, that is, 0.772 eV (surface entry), 0.555 eV (escape), and 0.828 eV (bulk diffusion), exceeding those of PA6 and PE. The unique behavior of PEF stems in part from its high bulk density, but more distinctively from the quasi-coplanar molecular traps formed by intrachain oxygen atoms that impede the movement of H_2 molecules. Despite the risks associated with cryogenic adsorption, the crystalline structure of α-PEF provides the basis for its remarkable hydrogen barrier properties, making it an excellent candidate for practical high-pressure hydrogen applications.

Keywords: PEF crystal; molecular simulation; hydrogen barrier; CVFF force field; gas transport

1. Introduction

Due to its high energy density, environmental benefits, and flexibility, hydrogen serves as an essential energy resource in storage, transportation, and industrial uses [1,2]. However, the high permeability and diffusivity present significant challenges for secure storage and transportation of hydrogen. Among the primary methods for high-pressure hydrogen storage, type IV cylinders are highly dependent on liner materials to prevent hydrogen leakage, improve storage efficiency, and ensure operational safety [3]. Despite the extensive use of petroleum-sourced polyamide 6 (PA6) and polyethylene (PE), these materials are limited in offering effective gas barriers, thermal stability, and mechanical strength [4]. Recently, biobased polyethylene furanoate (PEF), characterized by its distinctive furan ring structure, high density, and superior mechanical strength, has demonstrated enhanced gas barrier properties, making it a promising candidate for high-performance hydrogen storage applications [5–8]. However, the microscopic mechanisms that govern the hydrogen barrier performance of PEF remain incompletely understood, hindering its integration into hydrogen storage systems. Therefore, a detailed investigation of the hydrogen barrier mechanisms of PEF and its comparison with existing materials are essential for the advancement of novel and efficient hydrogen barrier technologies.

Type IV cylinders are typically designed to operate at temperatures ranging from -40 °C to +85 °C, with standard working pressures of 35 MPa or 70 MPa, and can withstand up to 125% of the designated pressure under extreme conditions [9]. Liner materials, which serve as critical sealing components in hydrogen storage tanks, must exhibit exceptionally low hydrogen permeability, excellent thermal stability, and robust mechanical integrity. In addition, they need to resist hydrogen embrittlement and prevent plastic deformation during rapid pressure fluctuations [9]. Semicrystalline HDPE is a common choice for hydrogen storage due to its low permeability and chemical stability; however, limited thermal resistance and poor interfacial adhesion reduce its effectiveness at elevated temperatures [4,10]. PA6, another semicrystalline material, has gained attention for its superior mechanical performance and thermal stability. Under conditions of 50 MPa and 25 °C, PA6 exhibits a hydrogen permeability coefficient approximately one-fifth that of HDPE [11]. However, PA6's high hygroscopicity makes it moisture sensitive, compromising the mechanical and gas barrier properties. As a result, PA6 is often incorporated into composites through blending or chemical modification to enhance its performance [12,13]. Moreover, since both HDPE and PA6 are petroleum-based, increasing sustainability concerns require the development of environmentally friendly hydrogen storage liner materials that maintain high performance and safety.

In recent years, PEF, a biobased polymer, has garnered significant interest as a sustainable alternative to conventional petroleum-based poly(ethylene terephthalate) (PET). This has led to extensive research comparing the two materials [14,15]. The foundational studies by Burgess *et al.* References [16–19] examined the sorption of oxygen, carbon dioxide, and water in amorphous and semicrystalline PEF and PET. Their results revealed that the rigid furan structure in amorphous PEF significantly restricts polymer chain mobility, leading to a much lower diffusion coefficient compared to PET. Additionally, increased crystallinity in semicrystalline PEF enhances its barrier properties by forming crystalline regions that serve as physical barriers, effectively prolonging the diffusion path. The higher crystallinity in PEF also results in a lower Henry's law adsorption parameter (k_D) for water and a decrease in the Langmuir capacity constant (C_{H0}), confirming that the crystalline domains act as barriers to gas permeation. Despite structural similarities at the monomer level, PEF and PET exhibit significant differences in barrier properties, prompting further research into the relationship between microstructure and barrier performance. Dimitriadis *et al.* [20] proposed a three-phase model to describe the microstructure of PEF, which consists of crystalline regions, mobile amorphous regions, and rigid amorphous regions (RAF) constrained by crystalline phases. In amorphous structures, reduced free volume and enhanced chain rigidity contribute to lower gas solubility and diffusion, thereby improving barrier performance. The rigid amorphous regions are also thought to play a critical role in enhancing gas barrier properties. However, these theoretical models require further validation through detailed investigations of molecular conformation and crystal structure.

Crystallization studies have shown that PEF can form into three polymorphic structures: α, α', and β, depending on crystallization conditions [21,22]. According to Stoclet *et al.* [21], the less ordered phase α' and the more ordered phase α form at crystallization temperatures below and above 170 °C, respectively. The β form, which is relatively unstable, is observed in solution crystallized samples [22,23]. Stoclet *et al.* [24,25] further explored the effect of mechanical stress on the crystalline structure of PEF, showing that the crystalline structure formed by stretching differs from thermally induced crystallization. However, subsequent work by Forestier *et al.* [26] indicated that strain-induced phases closely resemble those obtained through isothermal crystallization. Although slight angular differences exist between strain-induced crystallization (SIC) and static crystallization, these are probably due to extended chain conformations in SIC compared to stacked configurations in static crystallization. XRD studies by Mao *et al.* [27] proposed a monoclinic unit cell (within the $P2_1$ space group) with nearly planar polymer chains exhibiting staggered conformations, such as the 3/12 and 5/12 center-chain configurations, rejecting the earlier triclinic model suggested by Kazaryan *et al.* [28]. Maini *et al.* [29] later identified a form α' consistent with previous studies and described new structures for the α and β polymorphs, though Araujo *et al.* [7] subsequently refuted these models due to inconsistencies with molecular conformation principles.

Araujo *et al.* [7] combined vibrational spectroscopy with first-principles calculations to analyze the molecular conformation of PEF, identifying helical chain arrangements in the amorphous phase and extended zigzag conformations in the crystalline phase, stabilized by C-H$\cdots$O hydrogen bonds. Their findings provided a foundation for understanding the molecular conformations of PEF, highlighting the role of chain rigidity and limited ring flipping in improving barrier performance. Papamokos *et al.* [30] analyzed PEF's molecular conformation and proposed that helical formations in the amorphous state play a pivotal role in its gas barrier functionality. Sun *et al.* [8] pointed out that, beyond structural geometry, the high polarity of the furan ring enhances the performance of the PEF gas barrier by strengthening interactions with gas molecules, including CO_2. Zhao *et al.* [31] conducted a comparative study on the gas barrier properties of PEF, poly(propylene furanoate) (PPF) and poly(butylene furanoate) (PBF) against gases such as O_2 and CO_2 using both experimental methods and molecular simulations. Their results demonstrated the superior performance of PEF, in agreement with the findings of Wang *et al.* [32]. The intrinsic dipole characteristics of the furan group, combined with the restricted ring flipping because of its nonlinear rotation axis, enhance both chain rigidity and polarity, which are essential for improving the barrier properties of biobased polyesters. Lightfoot *et al.* [33] employed Molecular Dynamics (MD) and Grand Canonical Monte Carlo (GCMC) simulations on different amorphous and crystalline structures to successfully model oxygen diffusion coefficients, which corroborates the experimental data. They found that the rigidity and polarity of the furan ring of PEF reduce the chain mobility, decrease the free volume, and limit the connectivity of diffusion pathways, with crystalline domains acting as barriers to gas-molecule movement. They also highlighted the significant impact of PEF's density on the barrier properties. It should be noted that previous simulations were based on Mao's structure [27], which, although precise, does not represent the most stable form of PEF. Recently, Hoshide *et al.* [34] applied density functional theory (DFT) to optimize the α' phase into a monoclinic α crystal, thus providing theoretical confirmation of the atomic structure of α -PEF. This critical work offers valuable information for predicting and understanding the true barrier characteristics of PEF.

The structure of α-PEF and its superior barrier performance have initially been identified by molecular conformation analyzes, which emphasize its amorphous nature. However, a comprehensive understanding of the crystalline regions remains insufficient, particularly concerning how their inherent properties influence barrier performance. Traditionally, crystalline regions in polymeric materials have been oversimplified as either "extended diffusion pathways" or passive "physical barriers." However, advanced characterization reveals that these domains frequently contain structural defects (e.g., dislocations, grain boundaries) and exhibit complex morphological heterogeneity, while dynamic interactions at crystalline-amorphous interfaces further complicate their functional role in mass transport phenomena [35]. The current research paradigm has disproportionately emphasized PEF applications in food packaging, with insufficient attention to its promising characteristics for high-pressure hydrogen storage. Given that PA6, PE, and PEF all possess semicrystalline architectures, a systematic quantification of their hydrogen interaction mechanisms—particularly through crystallographic analysis of gas permeation pathways—could significantly enhance barrier performance predictions. Critical insights are expected to emerge from detailed investigations of crystal-amorphous interfacial dynamics [36].

Over the past five years, artificial intelligence (AI) and machine learning (ML) technologies have been increasingly integrated into the development and performance research of polymers [37–41]. However, data scarcity remains a primary obstacle hindering the broader application of ML in this field. Theoretical models represent a potential source of reliable data for training ML models. Yet, a unified model framework to quantitatively assess the impacts of the crystalline region on gas barrier performance remains critically lacking.

In this paper, MD simulations are employed in a unified force field framework to quantitatively compare the interaction strengths between crystalline PEF, PA6, PE and hydrogen molecules, aiming to elucidate the crystallographic origins of their differences in barrier performance. First, density functional theory (DFT) calculations are conducted to identify the most stable polymorph of PEF crystals for comparison with PA6 and PE and to generate reference data for force field development. Next, the CVFF force field is revised for PEF and validated by comparing key properties—such as lattice constants and surface energies—with DFT benchmarks for the three materials. Subsequently, MD simulations are carried out to evaluate the surface adsorption behavior of hydrogen on the three crystal types. Finally, nudged elastic band (NEB) calculations are used to characterize hydrogen migration pathways and quantify the energy barriers both within the crystalline bulk and across surface interfaces.

2. Model

In this study, all DFT calculations are performed using the Vienna Ab initio Simulation Package (VASP) [42] under periodic boundary conditions. The projector augmented wave (PAW) method [43] is used to describe electron-ion interactions, with a plane-wave energy cutoff of 550 eV. Exchange-correlation effects are treated within the generalized gradient approximation (GGA) using the Perdew-Burke-Ernzerhof (PBE) functional [44], while van der Waals interactions are taken into account by the DFT-D3 method with Becke-Johnson damping [45]. The Brillouin zone (BZ) is sampled using a $4 \times 4 \times 2$ Monkhorst-Pack k-mesh during geometry relaxation. Structural optimizations are performed under hydrostatic pressures ranging from -100 to 100 bar, with convergence thresholds set at 1×10^{-6} eV for total energy and 1×10^{-4} eV/Å for atomic forces. The core crystal structure of polyethylene furanoate (PEF) adopts the α-PEF framework proposed by Hoshide *et al.* [34]. For comparative analysis, the PEF structures reported by Mao *et al.* [27] and Maini *et al.* [29] are also examined. Reference structures for α-polyamide 6 (α-PA6) and α-polyethylene (α-PE) are taken from Quarti *et al.* [46] and Olsson *et al.* [47], respectively.

The molecular dynamics simulations in this study were conducted using the open-source software LAMMPS. The consistent valence force field (CVFF) [48,49] are selected for the polymer systems, which consists of four terms as follows:

$$E_{tot} = E_{vdwl} + E_{coul} + E_{long} + E_{mol} \tag{1}$$

where E_{vdwl} is the van der Waals term and calculated by the Lennard-Jones potentials, the coulombic term E_{coul} is calculated by the coulombic pairwise interaction, the long-range interaction term E_{long} is evaluated in K-space by the ewald style solver and the cutoff radius is set as 18.5 Å. E_{mol} is the local molecular term and comprehensively accounts for bond length, bond angle, dihedral torsion, and out-of-plane interactions.

In particular, while the CVFF potential provides complete structural parameters for polymers such as PA6 and PE, some of the parameters for furan rings and C=O functional groups in the local molecular term remain unavailable. To address these deficiencies, the missing parameters are optimized based on the DFT results and detailed results are presented in the Supplementary Material.

The crystal structural optimization simulations comprise two distinct processes: (1) NPT ensemble equilibration at $T = 1$ K and $P = 1$ atm for 10 ps, followed by (2) energy minimization using the conjugate gradient (CG) algorithm. The triclinic periodic boundary constraints are employed for PEF, PA6 and PE during crystal optimization.

For surface energy calculations, the simulation processes are similar, but vacuum layers are added in surface atomic models. The surface energy γ is calculated as follow:

$$E_{\text{surf}} = \frac{E_{\text{tot}} - N_{\text{atom}} E_{\text{bulk}}^{\text{per atom}}}{2A} \tag{2}$$

where N_{atom} denotes the atom count in the system, $E_{\text{bulk}}^{\text{per atom}}$ represents the per-atom energy in the bulk crystal state, and A is the surface area.

To quantify the H_2 adsorption energy (E_{ads}) on surfaces, hydrogen molecules are systematically positioned at vertical distances ($x = 1{\sim}3$ Å) above the optimized surface structure. The adsorption energy is defined thermodynamically as:

$$E_{\text{ads}} = E_{\text{surf+H}_2} - E_{\text{surf}} - E_{\text{H}_2} \tag{3}$$

where $E_{\text{surf+H}_2}$ represents the total energy of the surface-adsorbate system with H_2 at adsorption positions, E_{surf} denotes the energy of the fully relaxed surface, and E_{H_2} corresponds to the isolated hydrogen molecule energy in vacuum. The interaction energy in crystalline bulk systems is calculated in the similar way as:

$$E_{\text{inter}} = E_{\text{bulk+H}_2} - E_{\text{bulk}} - E_{\text{H}_2} \tag{4}$$

where $E_{\text{bulk+H}_2}$ includes the hydrogen molecule embedded in the periodic bulk lattice. During these calculations, the surface or bulk atoms are fixed while allowing relaxation of the H_2 molecule to ensure computational consistency.

To investigate the hydrogen diffusion mechanisms within the crystal lattice, we applied the NEB method and Grand canonical Monte Carlo (GCMC) simulations. In NEB simulation, the initial and final states are selected from the most stable H_2 adsorption or interaction sites. All NEB calculations maintain fixed unit cell dimensions while performing structural relaxation using the QuickMin algorithm. GCMC simulations are conducted on the basis of the relaxed surfaces. The simulation protocol initiates with a 10 ps NVT ensemble equilibration, followed by the determination of the excess chemical potential μ_{ex} using the Widom particle insertion methodology. The fundamental relationship governing this potential is expressed as:

$$\mu_{\text{ex}} = -k_{\text{B}} T \ln \left\langle \exp\left(-\frac{U_{N+1} - U_N}{k_{\text{B}} T} \right) \right\rangle \tag{5}$$

where U_N and U_{N+1} represent the potential energies of systems containing N and $N+1$ molecules respectively, k_B denotes the Boltzmann constant, and T is the temperature in Kelvin. Subsequent to chemical potential evaluation, the mass fraction-based Henry's law constant under infinite dilution conditions ($x_i \to 0$) , so called the sorption coefficient S_i, is calculated through:

$$S_i = \frac{M_i}{\rho_{\text{pol}} RT} \exp\left(\frac{\mu_i^{\text{ex}}}{RT}\right) \tag{6}$$

where ρ_{pol} corresponds to the polymer matrix density and M_i represents the molecular weight of the gaseous species.

3. Results and discussion

3.1. Benchmark

3.1.1. Thermodynamic stablity of PEF polymorphs

To confirm the thermodynamic stability ranking of α-PEF in PEF polymorphism, six configurations are optimized with DFT method, including α-PEF-2024 [34], α-PEF-2018 [29], α'-2018 [29], β-2018 [29], α_1-PEF-2016 (3/12 center chain-staggering) [27], and α_2-PEF-2016 (5/12 center chain-staggering) [27], as shown in Figure 1 and Table 1. The three-dimensional crystallographic analysis revealed the structures of α, α'-2018, α_1-2016, and α_2-2016 are all of monoclinic system $P2_1$ (c-axis unique). The optimized α-phase lattice parameters (a = 5.669 Å, b = 6.809 Å, c = 20.519 Å, γ = 107.398°) show excellent consistency with Hoshide's data [34], with relative differences of 0.91%, 0.87%, and 0.56% in a, b, and c, respectively, and a slight angular discrepancy of 0.13% in γ. The lattice parameters of other α phases also exhibit a minimal deviation from the α-phase and can generally be considered metastable phases. Regarding the β-phase, the results differ significantly from the established literature, particularly with the γ angle diverging from 90°. Moreover, the interaction between the furan ring and the diol does not match Araujo's preferred conformation of PEF chains in both crystalline ($syn^{\text{FDCA}} trans^{\text{EG}}$) and amorphous ($anti^{\text{FDCA}} gauche^{\text{EG}}$) states [7]. Despite the minor differences, therefore, our DFT-optimized configurations of PEF are consistent with the relevant literature reports [7,34].

Given the potential application of PEF in high-pressure environments, we further investigated the enthalpy variations of PEF polymorphs with DFT method across a pressure range from −100 bar to +100 bar, as illustrated in Figure 2. The enthalpy of all polymorphic phases increases steadily with pressure, exhibiting a degree of asymmetry between the tensile and compressive regimes. Throughout the range, the α phase consistently exhibits the lowest enthalpy, reaffirming its thermodynamic stability under pressure. In contrast, the phase β shows a markedly higher enthalpy than the other polymorphs, underscoring its thermodynamic instability. Among the metastable α polymorphs, the enthalpy ranking from highest to lowest follows the order: α_2-2016 > α_1-2016 > α'-2018. Specifically, the latter two structures are nearly degenerate in energy and are likely variations of the same metastable form, denoted as α'—a conclusion also supported by their similar crystal packing as shown in Figure 1. At high pressures (e.g., ±100 bar), the enthalpies of the two metastable phases nearly converge with that of the stable α phase, suggesting a stress-induced α' *to* α transition consistent with strain-induced crystallization [15].

Table 1. DFT-optimized lattice constants of PEF polymorphs.

PEF crystal	**a (Å)**	**b (Å)**	**c (Å)**	α **(°)**	β **(°)**	γ **(°)**	**Source**
α-phase	5.669 379	6.808 883	20.518 511	90	90	107.3977	This work
α-phase	5.618	6.750	20.404	90	90	107.26	[34]
α_1-phase	5.617 404	6.905 302	20.401 819	90	90	108.456 15	This work
α_2-phase	5.613 403	7.025 298	20.323 887	90	90	109.255 35	This work
$\alpha_{1/2}$-phase	5.784	6.780	20.296	90	90	103.3	[27]
α'-phase	5.652 243	6.863 814	20.455 74	89.990 54	89.9842	108.016 43	This work
α'-phase	5.912	6.91	19.73	90	90	104.41	[29]
β-phase	6.386 952	6.432 263	10.192 697	90.175 78	110.2932	84.652 82	This work
β-phase	5.953	6.60	10.52	90	107.0	90	[29]

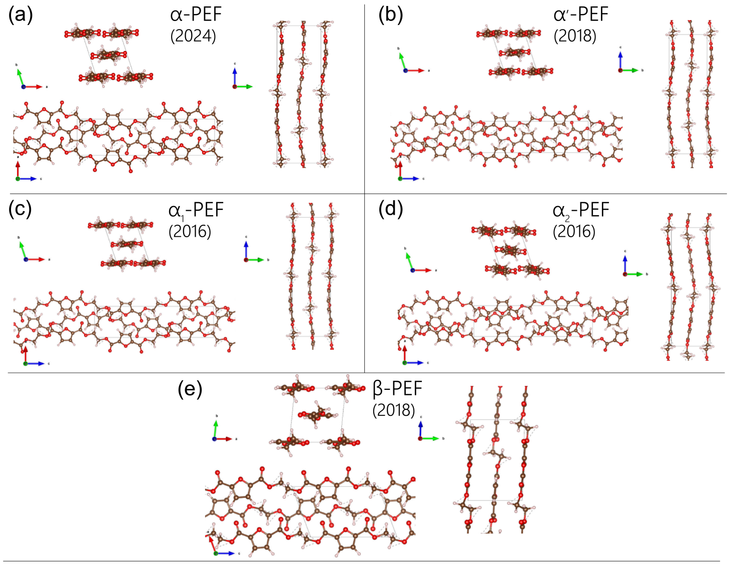

Figure 1. (Color online) DFT-optimized configurations of PEF polymorphs: **(a)** α-phase(2024); **(b)** α'-phase(2018); **(c)** α_1-phase(2016); **(d)** α_2-phase(2016); **(e)** β-phase(2018).

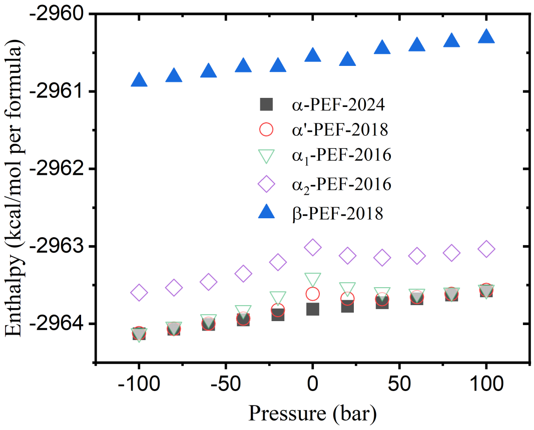

Figure 2. (Color online) Enthalpy of PEF polymorphs varing with pressures at 0 K.

3.1.2. Verification of the modified CVFF force field for α-PEF, α-PA6 and α-PE

Based on the proven stability of α-PEF by DFT, as well as the α-PA6 and α-PE structures verified in the literature [46,47], the rationality of the revised CVFF parameters given in the Supplementary Material will be examined in this section. Note that in the following content, the prefix α- will be omitted henceforth unless otherwise specified. First, the size dependence of the crystal lattice constants of the three materials was examined in MD simulations, as shown in Figure 3a. For each material we constructed six configurations, ranging from the unit cell ($1 \times 1 \times 1$) to supercells with dimensions from $2 \times 2 \times 2$ up to $6 \times 6 \times 6$, with the largest supercell containing 216 unit cells. The analysis reveals a size-dependent effect on the crystal structures across all materials. In PEF, MD simulations identified its triclinic structure, with significant variations in lattice constants a, b, and the angle γ observed up to a supercell size of $3 \times 3 \times 3$. In contrast, PA6 exhibited relatively minor fluctuations in lattice constants, achieving stability at a supercell size of $3 \times 3 \times 3$. For PE, structural stabilization occurs only in supercell sizes exceeding $4 \times 4 \times 4$. These findings highlight the necessity of selecting a sufficiently large supercell to ensure the accuracy of MD simulations for lattice parameters. To maintain consistency across the three materials, we adopted the $4 \times 4 \times 4$ supercell as the standard reference size.

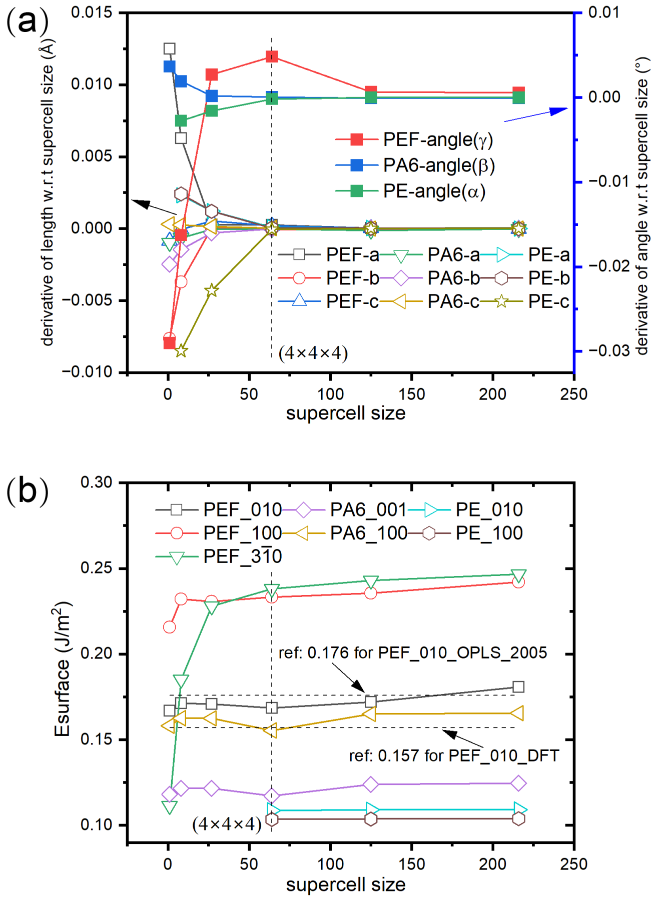

Figure 3. (Color online) **(a)** Derivative of lattice constants (length and angle) with respect to supercell size. **(b)** Variation of surface energy of different surfaces of PEF, PA6 and PE with supercell size.

To investigate the interaction of surfaces with H_2, a selection of representative stable surfaces was made, focusing on low-index orientations such as (100), (010) and (001). Unlike metal surfaces, polymer crystal surfaces, which are oriented along the chain direction, may exhibit dangling bonds, as observed in the (001) surface of PEF, the (010) surface of PA6, and the (001) surface of PE. These dangling bonds were omitted in the surface constructions. For accurate calculations, a supercell sensitivity analysis was conducted on the materials' surfaces, as shown in Figure 3b. The results indicate that as supercell sizes increase, the structures of different surfaces gradually converge. Notably, higher-index planes, such as PEF-$(3\bar{1}0)$ require larger supercells to achieve convergence. The surfaces, ranked by energy, follow the order: PEF-010 $>$ PA6-100 $>$ PE-100. Literature reports [33] indicate surface energies for PEF of 0.176 J/m^2 and 0.157 J/m^2 using the OPLS_2005 force field and DFT, respectively. Most of our PEF-010 surface energy data fall within this range, importantly, supporting the validity of our force field construction. To ensure consistency with bulk phase size effects, a $4 \times 4 \times 4$ surface supercell will be adopted in the subsequent study for both bulk and surface phases. Unless otherwise stated, the crystal planes referred to in the following sections are the three lowest energy surfaces determined here.

The MD-optimized lattice constants for the three crystals of α-PEF, PA6 and PE are listed in Table 2. For PA6 and PE, the calculations employed the original CVFF parameters, yielding results that exhibit excellent agreement with experimental data and the existing literature, particularly for PA6 [46]. Regarding PEF, the c lattice constant and γ angle align well with the DFT results, validating the effectiveness of the revised CVFF parameters. However, the a and b values for PEF deviate by more than 7%. This discrepancy is attributed to differences in molecular interactions as depicted in MD relative to DFT, leading to rotations of polymer chains within the a-b plane, as illustrated in Figure 4. For DFT, the chains are nearly orthogonal to the c-axis, with an inter-chain distance of 2.659 Å. Conversely, in the MD-optimized structure, the chains exhibit fluctuations and rotations, reducing the inter-chain spacing to 2.352 Å and tilting by nearly 10° from the original chain plane. Furthermore, when measured relative to the furan ring plane, the chain rotation angle is approximately 15°, corresponding to chain fluctuations. DFT analyses indicate that the dihedral angle between C1 and C2 in the furan ring is 177.81°, while MD simulations yield a dihedral angle between D1 and D2 of 175.81°, with a deviation of only 1.97°. These characteristics suggest that minor local adjustments in chain-like crystals can lead to significant overall variations. Due to lattice contraction, the density increases to 1.602 g/cm^3, compared to the experimental density of 1.562 g/cm^3 [27]. Given that the MD force field was parameterized solely based on DFT data of the PEF monomer, the close agreement with DFT benchmarks at the crystalline level validates the reliability of our force field, supporting its application in the subsequent quantitative comparison among the three materials.

Table 2. MD-optimized lattice constants of PEF, PA6 and PE.

Crystal	a (Å)	b (Å)	c (Å)	α (°)	β (°)	γ (°)	ρ (g/cm^3)	Source
α-PEF	5.232	7.284	20.972	90.003	90.000	109.160	1.602	This work
α-PA6	9.509	17.194	7.834	90.002	67.936	89.999	1.266	This work
α-PA6	9.560	17.240	8.010	90.000	67.500	90.000	1.305	Expt [46]
α-PA6	9.570	17.480	7.530	90.000	68.640	90.000	1.245	DFT-D [46]
α-PE	7.181	4.804	2.512	89.996	90.003	90.001	1.074	This work

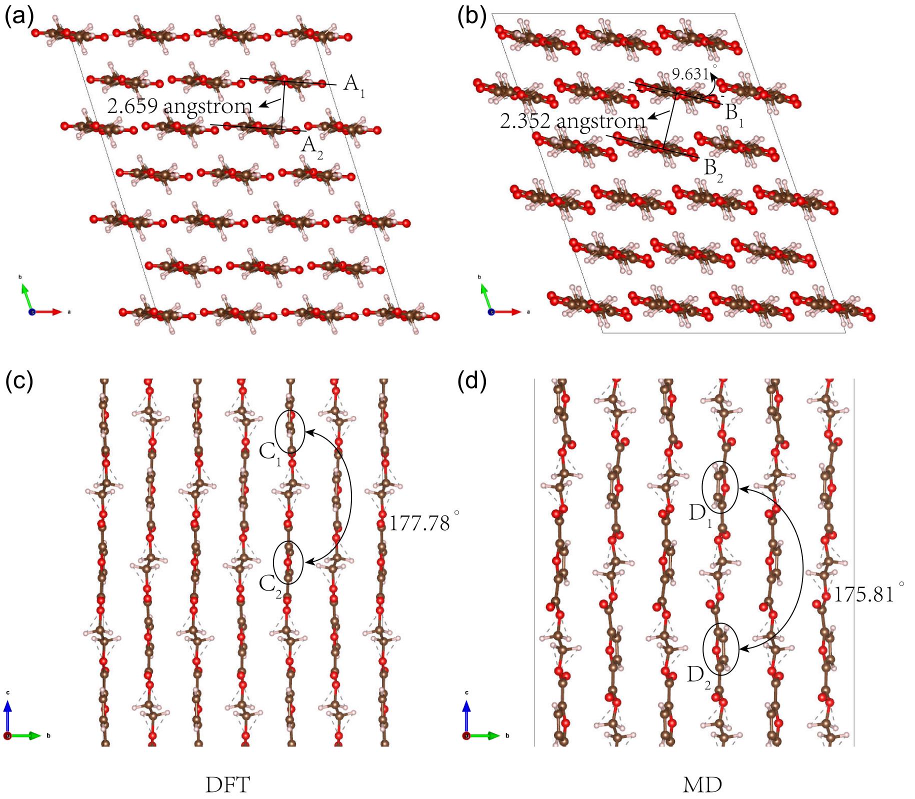

Figure 4. (Color online) Comparison of DFT optimized α-PEF structure (left side) with those from MD (right side), **(a,b)** are along the b-axis (chain-view), while **(c,d)** along a-axis (transverse-view).

3.2. Interaction of hydrogen with crystalline PEF, PA6 and PE

3.2.1. Surface hydrogen adsorption

By utilizing the previously identified lowest-energy surface configurations, we calculated the adsorption energies for H_2 and generated contour graphs of these energies with a initial height of 1 Å above the surface peaks, as shown in Figure 5. Typically, the adsorption distance exceeds 3 Å, aligning with the range of van der Waals interactions [50,51]. However, to evaluate the adsorption behavior of the three materials under more constrained conditions, we selected a closer separation of 1 Å. Overall, all three surfaces exhibit hydrogen adsorption, as evidenced by the negative values of E_{abs}. In particular, PEF demonstrates the most pronounced adsorption, although the maximum value remains below 0.1 eV, suggesting weak adsorption. As shown in Table 3, E_{vdwl} constitutes the dominant contribution in E_{abs} for all three crystal planes, indicating that the van der Waals interaction plays a predominant role. Remarkably, in PEF, the van der Waals contribution reaches 136%, while E_{mol} shows a counteracting contribution of -67%, demonstrating that physical adsorption dominates in PEF. This dominance causes local atomic displacements from equilibrium positions and induces structural adjustments. As shown in Figure 5, the primary adsorption sites in PEF are concentrated near oxygen atoms, due to their polarity and the formation of weak hydrogen bonds C-H$\cdots$O that moderately enhance adsorption [7]. Compared to oxygen-free PE, the coulombic effect of the O-H groups in PEF and PA6 contributes significantly (32% and 22%, respectively), the difference arising from their distinct surface oxygen densities. All three materials exhibit weak physical adsorption of hydrogen; however, PEF-010 demonstrates relatively stronger adsorption, mainly due to its high concentration of polar oxygen atoms, which enhance van der Waals and coulombic interactions with H_2.

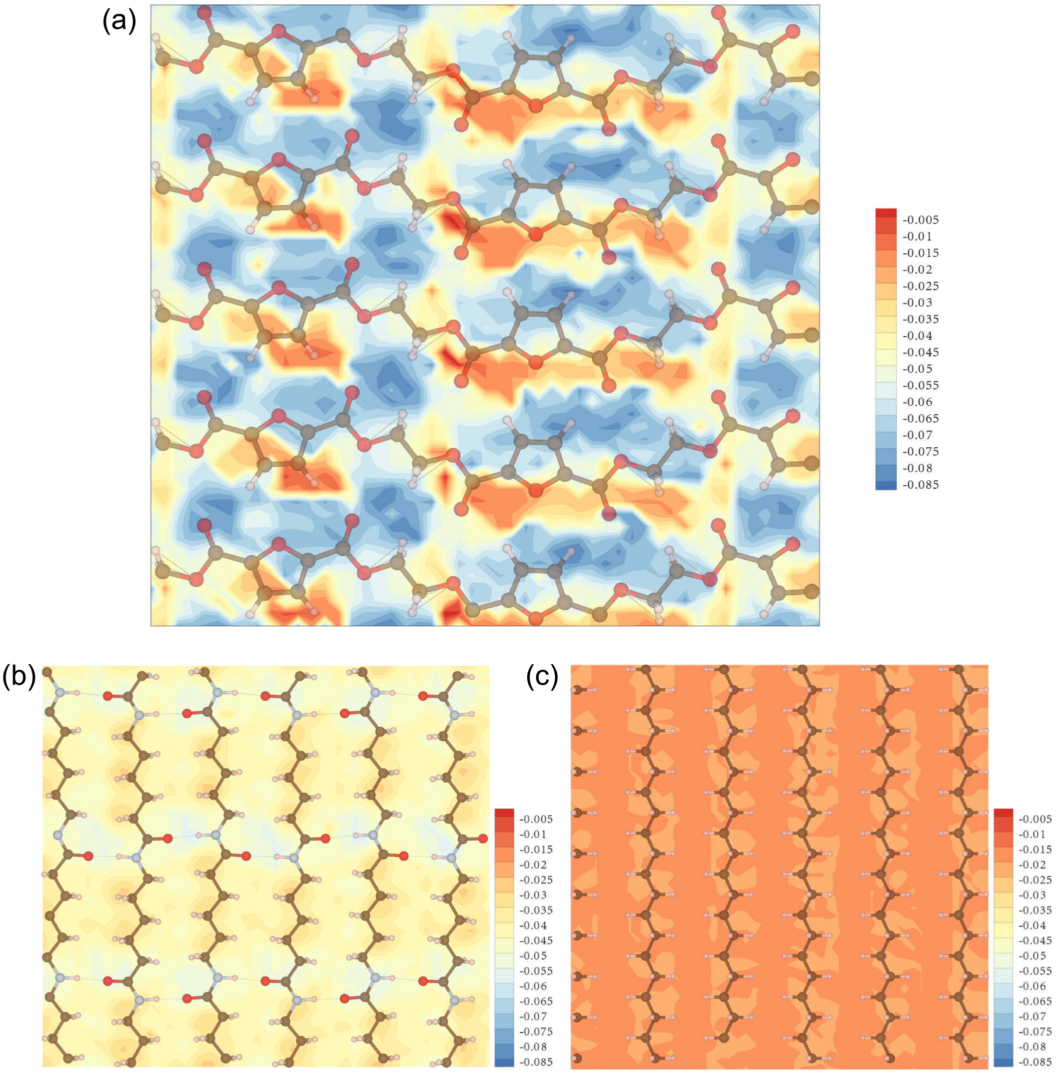

Figure 5. (Color online) MD-calculated surface adsorption energy contours (in eV) with the initial height 1 Å above the surface for **(a)** PEF-010, **(b)** PA6-001, and **(c)** PE-100.

Table 3. Components of the maximum H_2 adsorption energy E_{abs} (in eV) and their contributions for PEF-010, PA6-001 and PE-100 surfaces.

Crystal surface	E_{abs}	E_{vdwl}	E_{coul}	E_{long}	E_{mol}
PEF-010	−0.086648	−0.118134	−0.027897	0.000572	0.058615
PA6-001	−0.059766	−0.051490	−0.013250	0.000263	0.005207
PE-100	−0.026276	−0.027079	0.000994	−0.000022	−0.000140

To evaluate the adsorption capacities of these materials under varying temperatures and pressures, the excess chemical potential μ_{ex} was calculated and used to deduce the mass fraction-based Henry's constant S_i via Equation (6) over a temperature range of 223.15 K to 373.15 K, as shown in Figure 6. For consistency, all metrics related to surface adsorption were normalized by surface area. Considering that there is no free volume inside the crystal plane and hydrogen cannot dissolve inside, the adsorption at this time is reasonable to be described by Henry's law [52]. The results indicate that PEF has the highest μ_{ex} and S_i, followed by PA6 and PE, the latter two showing relatively similar values. The adsorption of PEF is more obvious at low temperatures, which is one order of magnitude higher than that of the other materials. However, as the temperature increases, S_i decreases sharply and the disparity between the three materials decreases rapidly. At 373.15 K, the S_i values for PEF, PA6, and PE reach 0.00668, 0.00484, and 0.00441 MPa^{-1}, respectively, converging to nearly identical levels. Considering the excellent thermal stability and high glass transition temperature (T_g) of its semicrystalline form [53], PEF may exhibit superior potential for high-temperature applications compared to PE and PA6.

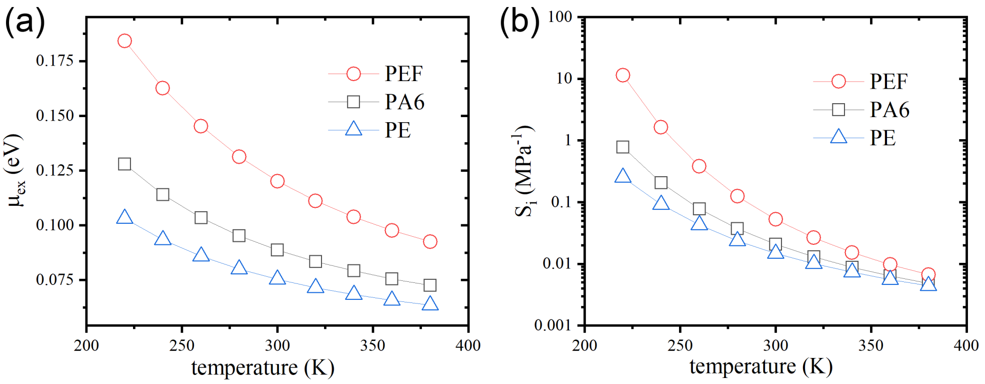

Figure 6. (Color online) **(a)** Excess chemical potential μ_{ex} of H_2 at dilute solution and **(b)** mass-fraction-based Henry's constants varying with temperature for the surfaces of PEF-010, PA6-001 and PE-100.

It is interesting to clarify the relationship between S_i and the density of the polymer ρ_{pol}. While Equation (6) suggests an inverse proportionality between S_i and ρ_{pol}, the calculated results paradoxically maintain the density order, that is, PEF $>$ PA6 $>$ PE. More plausibly, the surface adsorption properties of PEF should not be directly attributed to the bulk density but rather to the high concentration of polar oxygen atoms on the surface, analogous to the analysis of adsorption energy by MD calculation, as shown in Table 3. If semicrystalline PEF is exposed to extreme low-temperature and high-pressure conditions, it may experience excessive hydrogen adsorption on its crystal surfaces, potentially leading to local accumulation and swelling. However, the inherent rigidity of the crystalline domains and adjacent RAF regions [48] may help mitigate these effects. It is important to note that the above analysis is derived purely from a crystallographic perspective. In practical PEF materials, the amorphous regions, with their larger free volume, serve as the primary sites for hydrogen uptake. Therefore, a more accurate prediction of overall barrier performance would require consideration of these amorphous contributions, which, however, is beyond the scope of this study.

3.2.2. Hydrogen migration energy barriers

Although the adsorption analysis suggests that H_2 does not have solubility within the crystal under thermodynamic equilibrium, NEB calculations of bulk diffusion and surface penetration remain crucial to understanding the interactions between hydrogen and the crystal under non-equilibrium conditions. We first performed MD-based interaction energy scans of H_2 within the crystalline bulk of the three materials, as illustrated in Figure 7. Specifically, Figure 7a,c,e shows the energy slice taken from the central region parallel to the most stable crystallographic plane for each material, overlaid with atoms from the adjacent upper and lower layers (with greater transparency for the upper layer). The results showed that all interaction energies were positive, suggesting that additional energy is required for H_2 adsorption within the crystals. The energy profiles indicated that PE had the highest interaction energy, with an average interatomic interaction energy per unit cell of $\delta_{\text{inner}}^{\text{PE}} = 8.36 \times 10^{-4}$ eV. In comparison, PA6 showed $\delta_{\text{inner}}^{\text{PA6}} = 5.62 \times 10^{-4}$ eV, while PEF recorded the lowest value with $\delta_{\text{inner}}^{\text{PEF}} = 2.23 \times 10^{-4}$ eV. As shown in Figure 7b, the lowest energy structures revealed that PEF adopts a nearly planar configuration involving H_2 and four oxygen atoms from neighboring chains, with the closest H_2-oxygen distance being approximately 2.4 Å. In contrast, PA6 and PE achieved their lowest energy states through interactions with adjacent hydrogen atoms, at distances of about 2.0 Åand 1.6 Å, respectively, with the latter experiencing significant repulsion.

Based on the low-energy configurations scanned, we further performed MD-based NEB calculations along the three principal crystallographic directions: normal (perpendicular to the lowest energy surface), chain (along the polymer backbone), and transverse (the third direction) for all three materials, as shown in Figure 8a. This directional labeling ensures a consistent comparison across different crystal systems. The barrier of PEF was highest in the transverse direction at 1.105 eV, followed by the normal direction at 0.733 eV, and smallest along the chain direction at 0.646 eV. For PA6, the maximum energy barrier occurred in the normal direction, while the minimum was also along the chain direction, which is the same as PEF. For PE, results in normal and transverse directions were not obtained due to molecular obstruction, with only the chain direction barrier available, showing a notably low value of 0.032 eV. According to the NEB results for intracrystalline diffusion by MD, in summary, PEF exhibited the highest energy barriers across all three paths.

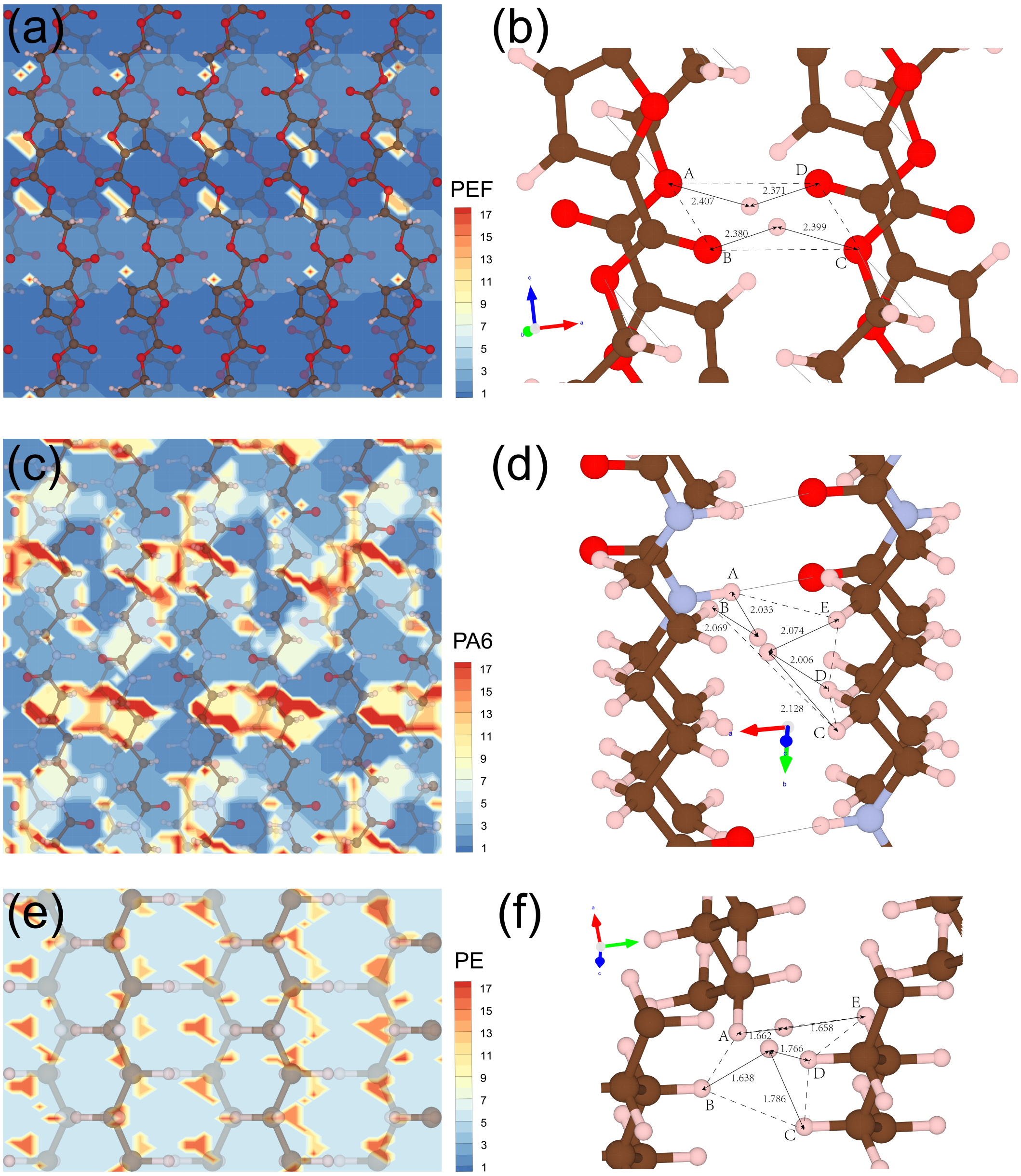

Figure 7. (Color online) MD-calculated interaction energy of H_2 with **(a)** PEF, **(c)** PA6 and **(e)** PE; the local structure with minimum interaction energy for **(b)** PEF, **(d)** PA6 and **(f)** PE.

To validate the MD results, NEB simulations of H_2 diffusion in PEF-100 and PEF-010 were repeated using DFT within a unit cell. The resulting energy barriers are 0.890 eV and 0.764 eV, respectively. Compared to DFT, MD overestimates the barrier in the [100] direction by 24%, while the deviation in the [010] direction is only 4%. This overestimation likely stems from the insufficiently smooth description of the MD force field of the chain segments along [100], as illustrated in Figure 4a,b, where the distance between the furan rings in MD is shorter than in DFT, leading to stronger van der Waals repulsion during H_2 migration. In contrast, the [010] direction is less sensitive to this structural discrepancy, resulting in closer agreement with DFT. For convenience in comparison, the average value of the MD-calculated NEB barriers is adopted as the characteristic diffusion barrier, as summarized in Table 4. The average barrier of PEF (0.828 eV) is 2.9 times higher than that of PA6 (0.287 eV) and 25.9 times that of PE (0.032 eV). In addition, DFT calculations also show that the charge transfer during hydrogen diffusion is basically between 0.03e and 0.07e, indicating that the interaction between H_2 and PEF is weak and no chemical reaction is possibly involved. Therefore, it is reasonable to conclude that H_2 diffusion within the crystals shares a mechanism similar to that of surface adsorption, both of which are predominantly governed by physical interactions.

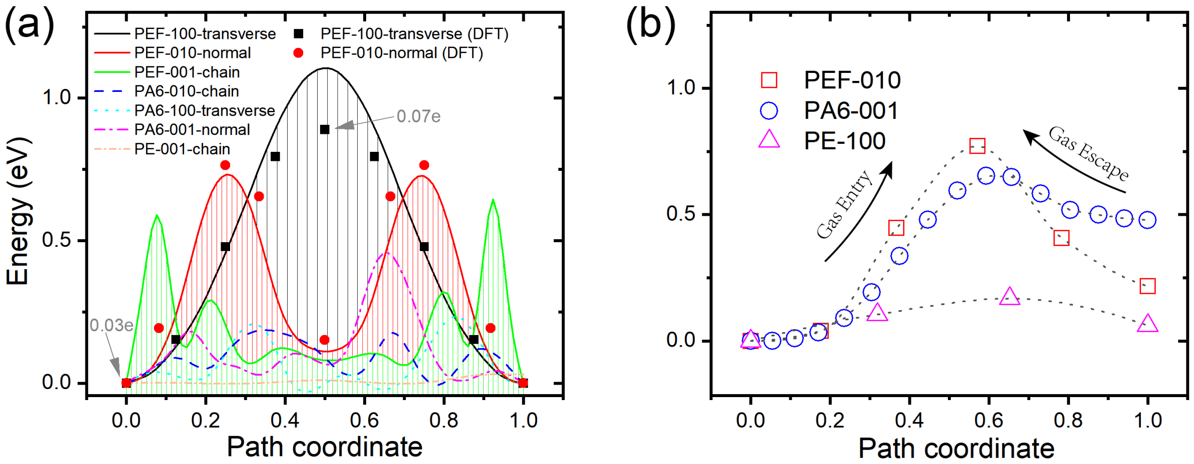

Figure 8. (Color online) Calculated energy barriers of H_2 in the **(a)** bulk and **(b)** surfaces of PEF, PA6 and PE. Most of the results are obtained by MD calculations, except for two paths (indicated by solid scattered box or circle) which are obtained by DFT. The unit *e* represents the amount of electron transfer.

Table 4. MD-calculated NEB energy barriers of H_2 in PEF, PA6, and PE polymer crystals.

Crystal	**Bulk (eV)**				**Surface (eV)**	
	Chain	**Normal**	**Transverse**	**Average**	**Entry**	**Escape**
PEF	0.646	0.733	1.105	0.828	0.772	0.555
PA6	0.175 (3.7 ×)	0.454 (1.6 ×)	0.233 (4.7 ×)	0.287 (2.9 ×)	0.654 (1.2 ×)	0.175 (3.2 ×)
PE	0.032 (20.2 ×)	–	–	0.032 (25.9 ×)	0.167 (4.6 ×)	0.106 (5.2 ×)

To assess the hydrogen barrier performance of the three materials—including both inward penetration and outward escape—NEB simulations were conducted via MD for PEF-010, PA6-001, and PE-100, as shown in Figure 8b. In all cases, the energy at the initial coordinate (0.0) was lower than at the final coordinate (1.0), indicating that hydrogen surface penetration is non-spontaneous and requires an external driving force, consistent with the previously reported positive intracrystalline interaction energies as shown in Figure 7. The entry and escape barriers are defined as the energy differences between the peak and the initial or final states, respectively. Notably, the peak position is material-specific and not fixed at the midpoint (0.5). While PEF and PA6 exhibit comparable entry barriers, PEF's escape barrier is more than three times higher than that of PA6, as summarized in Table 4. PE, by contrast, shows the lowest entry and escape barriers among the three.

PEF exhibits the highest energy barriers for both surface penetration and internal diffusion of H_2, primarily due to van der Waals interactions between hydrogen molecules and the polymer matrix. These migration barriers are strongly influenced by the extent and nature of H_2 interactions with the surrounding atoms. Among the three materials studied, PEF possesses the highest atomic packing density, which enhances the frequency and strength of short-range interactions acting on diffusing H_2, thereby significantly increasing the diffusion barrier. Furthermore, PEF forms a particularly stable low-energy configuration through coordinated interactions between H_2 and four oxygen atoms from neighboring chains. This structural feature contributes to the elevated energy barriers for both internal diffusion and surface escape. Together, the dense molecular packing and specific polar interactions offer a comprehensive explanation for PEF's superior barrier performance, underscoring the crucial influence of nanoscale structural characteristics on gas transport behavior in semicrystalline polymers.

4. Conclusion

In this study, we have employed MD simulations with a modified CVFF force field to systematically compare the hydrogen barrier properties of α-PEF, α-PA6, and α-PE from a crystallographic perspective. To establish an evaluation framework for polymer gas barrier properties, a unified model integrating crystal polymorphism analysis, intermolecular interaction mechanisms, surface-mediated gas adsorption and diffusion dynamics is developed. This model enables quantitative analysis of crystallographic properties and barrier performance, while also generating reliable data for machine learning models to establish the relationship between atomic structure and H_2 storage performance. The main findings are summarized as follows:

Among the three materials, the surface energy ranking of the most stable crystal planes follows PEF-010 $>$ PA6-001 $>$ PE-100, likely reflecting the denser atomic packing in PEF. All materials exhibit weak physical adsorption of H_2, with PEF showing the highest adsorption due to enhanced van der Waals and coulombic interactions from its oxygen-rich surface. However, thermal attenuation reduces the adsorption disparities, converging the three materials to comparable levels at elevated temperatures (e.g., 100°C). According to NEB calculations, particularly, PEF consistently possesses the highest H_2 migration barriers. Specifically, the surface gas entry barrier of PEF is 0.772 eV, slightly higher than that of PA6, both the escape barrier (0.555 eV) and the average bulk diffusion barrier (0.828 eV) are much higher than the other two materials. The unique behavior of PEF stems in part from its high bulk density, but more distinctively from the quasi-coplanar molecular traps formed by intrachain oxygen atoms that impede the movement of H_2 molecules. Note that polar oxygen atoms in PEF exhibit strong physical interactions with H_2 at both the surface and bulk levels, but their contributions to the behavior of the hydrogen barrier vary accordingly. Understanding the dual role of polar oxygen atoms deepens understanding of the barrier properties of PEF and offers guidance for their effective modulation.

Finally, despite the risk of enhanced hydrogen adsorption at low temperatures, the high crystallographic density and abundant polar oxygen atoms as well as the thermal stability and mechanical strength endow PEF with exceptional intrinsic barrier performance [34], laying a solid foundation for its application in high-pressure hydrogen environments. Given the semicrystalline nature of PEF, future research should focus on the influence of crystal defects and crystal–amorphous interfaces on overall barrier properties.

Supplementary data

The authors confirm that the supplementary data are available within this article.

Acknowledgments

The authors acknowledge the support of the Yangtze Delta Region Institute (Huzhou) Guidance Fund of University of Electronic Science and Technology of China (Grant No. U03250002), the National Natural Science Foundations of China (Grant No. 12105066), Ningbo Polytechnic high-level talent introduction research project, Ningbo Polytechnic Academician Workstation.

Authors' contribution

Conceptualization, Yaolin Guo and Yajie Zhang; methodology, Zhen Liu and Yaolin Guo; software, Zhen Liu and Yaolin Guo; validation, Zhen Liu, Yaolin Guo and Bin Gu; formal analysis, Zhen Liu; investigation, Zhen Liu and Yaolin Guo; resources, Yaolin Guo; data curation, Zheyu Hu; writing—original draft preparation, Zhen Liu and Yaolin Guo; writing—review and editing, Bin Gu, Nianxiang Qiu, Xiaojing Bai, Yifan Li, Zheyu Hu, Muhammad Adnan and Yajie Zhang; visualization, Yifan Li; supervision, Yaolin Guo; project administration, Yaolin Guo; funding acquisition, Nianxiang Qiu. All authors have read and agreed to the published version of the manuscript.

Conflicts of interests

The authors declare no conflict of interest.

References

[1] Mulky L, Srivastava S, Lakshmi T, Sandadi ER, Gour S, *et al.* An overview of hydrogen storage technologies—key challenges and opportunities. *Mater. Chem. Phys.* 2024, 325:129710.

[2] Li X, Dong C, Liu Y, Li J, Bin G, *et al.* Study on the effect of hydrogen cycle pressure relief time on the hydrogen permeability and mechanical properties of polyamide liner materials for type IV hydrogen storage cylinders of HFCVs. *Int. J. Hydrogen Energy* 2024, 95:993–1003.

[3] Hafner T, Macher J, Brandstätter S, Trattner A. Advancing hydrogen storage: development and verification of a high-pressure permeation test setup for polymeric barrier materials. *Int. J. Hydrogen Energy* 2024, 96:882–891.

[4] Wang X, Chen X, Yang J, Xie P, Yang W. Research on torsional laminated extrusion for improving the permeability and mechanical properties of HDPE/PA6 composite for type IV storage tank liners. *J. Appl. Polym. Sci.* 2023, 140(42):e54567.

[5] Burgess SK, Leisen JE, Kraftschik BE, Mubarak CR, Kriegel RM, *et al.* Chain mobility, thermal, and mechanical properties of poly(ethylene furanoate) compared to poly(ethylene terephthalate). *Macromolecules* 2014, 47(4):1383–1391.

[6] Burgess SK, Mubarak CR, Kriegel RM, Koros WJ. Physical aging in amorphous poly(ethylene

furanoate): enthalpic recovery, density, and oxygen transport considerations. *J. Polym. Sci., Part B: Polym. Phys.* 2015, 53(6):389–399.

[7] Araujo CF, Nolasco MM, Ribeiro-Claro PJA, Rudi´c S, Silvestre AJD, *et al.* Inside PEF: chain conformation and dynamics in crystalline and amorphous domains. *Macromolecules* 2018, 51(9):3515–3526.

[8] Sun L, Wang J, Mahmud S, Jiang Y, Zhu J, *et al.* New insight into the mechanism for the excellent gas properties of poly(ethylene 2,5-furandicarboxylate) (PEF): role of furan ring's polarity. *Eur. Polym. J.* 2019, 118:642–650.

[9] Kis DI, Kókai E. A review on the factors of liner collapse in type IV hydrogen storage vessels. *Int. J. Hydrogen Energy* 2024, 50:236–253.

[10] Kim M, Lee CH. Hydrogenation of high-density polyethylene during decompression of pressurized hydrogen at 90 MPa: a molecular perspective. *Polymers* 2023, 15(13):2880.

[11] Sun Y, Lv H, Zhou W, Zhang C. Research on hydrogen permeability of polyamide 6 as the liner material for type IV hydrogen storage tank. *Int. J. Hydrogen Energy* 2020, 45(46):24980–24990.

[12] Dong C, Liu Y, Li J, Bin G, Zhou C, *et al.* Hydrogen permeability of polyamide 6 used as liner material for type IV on-board hydrogen storage cylinders. *Polymers* 2023, 15(18):3715.

[13] Li J, Zhao X, Liang J, Zhao C, Feng N, *et al.* Molecular dynamics simulation of hydrogen barrier performance of modified polyamide 6 lining of IV hydrogen storage tank with graphene. *Polymers* 2024, 16(15):2185.

[14] Forestier E, Combeaud C, Guigo N, Corvec G, Pradille C, *et al.* Comparative analysis of the mechanical behaviour of PEF and PET uniaxial stretching based on the time/temperature superposition principle. *Polymers* 2021, 13(19):3295.

[15] Forestier E, Combeaud C, Guigo N, Sbirrazzuoli N, Billon N. Understanding of strain-induced crystallization developments scenarios for polyesters: comparison of poly(ethylene furanoate), PEF, and poly(ethylene terephthalate), PET. *Polymer* 2020, 203:122755.

[16] Burgess SK, Karvan O, Johnson JR, Kriegel RM, Koros WJ. Oxygen sorption and transport in amorphous poly(ethylene furanoate). *Polymer* 2014, 55(18):4748–4756.

[17] Burgess SK, Mikkilineni DS, Yu DB, Kim DJ, Mubarak CR, *et al.* Water sorption in poly(ethylene furanoate) compared to poly(ethylene terephthalate). Part 1: equilibrium sorption. *Polymer* 2014, 55(26):6861–6869.

[18] Burgess SK, Kriegel RM, Koros WJ. Carbon dioxide sorption and transport in amorphous poly(ethylene furanoate). *Macromolecules* 2015, 48(7):2184–2193.

[19] Burgess SK, Wenz GB, Kriegel RM, Koros WJ. Penetrant transport in semicrystalline poly(ethylene furanoate). *Polymer* 2016, 98:305–310.

[20] Dimitriadis T, Bikiaris DN, Papageorgiou GZ, Floudas G. Molecular dynamics of poly(ethylene-2,5-furanoate) (PEF) as a function of the degree of crystallinity by dielectric spectroscopy and calorimetry molecular dynamics of poly(ethylene-2,5-furanoate) (PEF) as a function of the degree of crystallinity by dielectric spectroscopy and calorimetry. *Macromol. Chem. Phys.* 2016, 217(18):2056–2062.

[21] Stoclet G, Gobius du Sart G, Yeniad B, de Vos S, Lefebvre JM. Isothermal crystallization and structural characterization of poly(ethylene-2,5-furanoate). *Polymer* 2015, 72:165–176.

[22] Tsanaktsis V, Papageorgiou DG, Exarhopoulos S, Bikiaris DN, Papageorgiou GZ. Crystallization and polymorphism of poly(ethylene furanoate). *Cryst. Growth Des.* 2015, 15(11):5505–5512.

[23] Lotti N, Munari A, Gigli M, Gazzano M, Tsanaktsis V, *et al.* Thermal and structural response of in situ prepared biobased poly(ethylene 2,5-furan dicarboxylate) nanocomposites. *Polymer* 2016, 103:288–298.

[24] Stoclet G, Lefebvre JM, Yeniad B, Gobius du Sart G, de Vos S. On the strain-induced structural evolution of poly(ethylene-2,5-furanoate) upon uniaxial stretching: an *in-situ* SAXS-WAXS study. *Polymer* 2018, 134:227–241.

[25] Stoclet G, Arias A, Yeniad B, De Vos S. Relationships between crystalline structure and the thermal behavior of poly(ethylene 2,5-furandicarboxylate): an *in situ* simultaneous SAXS-WAXS study. *Polym. Eng. Sci.* 2019, 59(8):1667–1677.

[26] Forestier E, Combeaud C, Guigo N, Monge G, Haudin JM, *et al.* Strain-induced crystallization of poly(ethylene 2,5-furandicarboxylate). Mechanical and crystallographic analysis. *Polymer* 2020, 187:122126.

[27] Mao Y, Kriegel RM, Bucknall DG. The crystal structure of poly(ethylene furanoate). *Polymer* 2016, 102:308–314.

[28] Kazaryan L, Medvedeva F. X-ray study of poly(ethylene furan-2, 5-dicarboxylate) structure. *Vysokomol. Soedin. Ser.* 1968, 10:305,306.

[29] Maini L, Gigli M, Gazzano M, Lotti N, Bikiaris DN, *et al.* Structural investigation of poly(ethylene furanoate) polymorphs. *Polymers* 2018, 10(3):296.

[30] Papamokos G, Dimitriadis T, Bikiaris DN, Papageorgiou GZ, Floudas G. Chain conformation, molecular dynamics, and thermal properties of poly(*n*-methylene 2,5-furanoates) as a function of methylene unit sequence length. *Macromolecules* 2019, 52(17):6533–6546.

[31] Zhao M, Zhang C, Yang F, Weng Y. Gas barrier properties of furan-based polyester films analyzed experimentally and by molecular simulations. *Polymer* 2021, 233:124200.

[32] Wang X, Cai X, Zhang X, Wang J, Zhu J. Bio-based high gas barrier polyesters based on furandicarboxylic acid: trade-off between ethylene and propylene diols. *Eur. Polym. J.* 2023, 197:112362.

[33] Lightfoot JC, Buchard A, Castro-Dominguez B, Parker SC. Comparative study of oxygen diffusion in polyethylene terephthalate and polyethylene furanoate using molecular modeling: computational insights into the mechanism for gas transport in bulk polymer systems. *Macromolecules* 2022, 55(2):498–510.

[34] Hoshide M, Kawasaki H, Abe S, Iwabuchi S, Kogure S, *et al.* Insights into conformation, crystal structure, and material properties of plant-derived poly(alkylene 2,5-furandicarboxylate)s as sustainable alternatives to petroleum-derived analogues. *Macromolecules* 2024, 57(13):6233–6247.

[35] Guinault A, Messin T, Anderer G, Krawielitzki S, Sollogoub C, *et al.* Relationship between crystallization, mechanical and gas barrier properties of poly(ethylene furanoate) (PEF) in multinanolayered PLA-PEF and PET-PEF films. In *Esaform 2021*, Liège, Belgium, April 14–16, 2021.

[36] Kumar M. Investigation of hydrogen transport properties through the liner material of 70 MPa type IV composite overwrapped pressure vessels. *Int. J. Pressure Vessels and Piping* 2024, 208:105150.

[37] Cao X, Zhang Y, Sun Z, Yin H, Feng Y. Machine learning in polymer science: a new lens for physical and chemical exploration. *Prog. Mater Sci.* 2026, 156:101544.

[38] Ge W, Silva R, Fan Y, Sisson S, Stenzel M. Machine learning in polymer research. *Adv. Mater.* 2025, 37(11):2413695.

[39] Song H, Li F, Li B, Guo J, Zhang W, *et al.* Research on the wellbore cleaning mechanism and prediction of cleaning ability of well-flushing fluid based on experiment-molecular dynamics simulation-machine learning. *Sep. Purif. Technol.* 2025, 359:130875.

[40] Song H, Li F, Li B, Guo J, Li J, *et al.* Flow law of particles carried by well-flushing fluid in the annulus and prediction of flushing efficiency based on numerical simulation-interpretable machine learning model. *Fuel* 2025, 392:134829.

[41] Song H, Ye Y, Zheng W, Bibiche EEAF, Zhang Q, *et al.* Synthesis of nano--CD@Fe3O4 magnetic material and its application in ultrasonic treatment of oily sludge. *Ultrason. Sonochem.* 2022, 92:106256.

[42] Kresse G, Furthmüller J. Efficient iterative schemes for Ab initio total-energy calculations using a plane-wave basis set. *Phys. Rev. B* 1996, 54(16):11169–11186.

[43] Kresse G, Joubert D. From ultrasoft pseudopotentials to the projector augmented-wave method. *Phys. Rev. B* 1999, 59(3):1758–1775.

[44] Perdew JP, Burke K, Ernzerhof M. Generalized gradient approximation made simple. *Phys. Rev. Lett.* 1996, 77(18):3865–3868.

[45] Caldeweyher E, Bannwarth C, Grimme S. Extension of the D3 dispersion coefficient model. *J. Chem. Phys.* 2017, 147(3):34112.

[46] Quarti C, Milani A, Civalleri B, Orlando R, Castiglioni C. Ab initio calculation of the crystalline structure and IR spectrum of polymers: nylon 6 polymorphs. *J. Phys. Chem. B* 2012, 116(28):8299–8311.

[47] Olsson PAT, Schröder E, Hyldgaard P, Kroon M, Andreasson E, *et al.* Ab initio and classical atomistic modelling of structure and defects in crystalline orthorhombic polyethylene: twin boundaries, slip interfaces, and nature of barriers. *Polymer* 2017, 121:234–246.

[48] Asensio JL, Martin-Pastor M, Jimenez-Barbero J. The use of CVFF and CFF91 force fields in conformational analysis of carbohydrate molecules. comparison with AMBER molecular mechanics and dynamics calculations for methyl α-lactoside. *Int. J. Biol. Macromol.* 1995, 17(3):137–148.

[49] Hobza P, Kabeláč M, Šponer J, Mejzlík P, Vondrášek J. Performance of empirical potentials (AMBER, CFF95, CVFF, CHARMM, OPLS, POLTEV), semiempirical quantum chemical methods (AM1, MNDO/M, PM3), and Ab initio hartree–fock method for interaction of DNA bases: comparison with nonempirical beyond Hartree–Fock results. *J. Comput. Chem.* 1997, 18(9):1136–1150.

[50] Karasawa N, William A Goddard III. Force fields, structures, and properties of Poly(vinylidene fluoride) crystals. *ACS Publications* 2002, 25(26):7268–7281.

[51] Hong SJ, Chun H, Lee J, Kim BH, Seo MH, *et al.* First-principles-based machine-learning molecular dynamics for crystalline polymers with van Der Waals interactions. *J. Phys. Chem. Lett.* 2021, 12(25):6000–6006.

[52] Smith ZP, Tiwari RR, Murphy TM, Sanders DF, Gleason KL, *et al.* Hydrogen sorption in polymers for membrane applications. *Polymer* 2013, 54(12):3026–3037.

[53] Codou A, Moncel M, van Berkel JG, Guigo N, Sbirrazzuoli N. Glass transition dynamics and

cooperativity length of poly(ethylene 2,5-furandicarboxylate) compared to poly(ethylene terephthalate). *Phys. Chem. Chem. Phys.* 2016, 18(25):16647–16658.